Research Square

Preprints are preliminary reports that have not undergone peer review.
They should not be considered conclusive, used to inform clinical practice,
or referenced by the media as validated information.

# Phase-averaging of temporally uncorrelated PIV snapshots using Input/Output analysis

**Joseph W. Nichols**

jwn@umn.edu

University of Minnesota

**Raphael Ribeiro**

University of Minnesota

**Melissa A. Green**

University of Minnesota

**Ellen K. Longmire**

University of Minnesota

**Research Article**

**Keywords:**

**Posted Date:** November 9th, 2026

**DOI:** https://doi.org/10.21203/rs.3.rs-11443593/v1

**License:** This work is licensed under a Creative Commons Attribution 4.0 International License.
Read Full License

**Additional Declarations:** Competing interest reported. Ellen Longmire is an editor-in-chief for Experiments in Fluids.

# Phase-averaging of temporally uncorrelated PIV snapshots using Input/Output analysis

Joseph W. Nichols[1*], Raphael Ribeiro[1], Melissa A. Green[1], Ellen K. Longmire[1]

[1*]Aerospace Engineering and Mechanics Department, University of Minnesota, Minneapolis, 55455, Minnesota, USA.

*Corresponding author(s). E-mail(s): jwn@umn.edu;
Contributing authors: ; ; ;

**Abstract**

We present a method to estimate a flow's spectral content from temporally uncorrelated PIV snapshots by projecting them onto bases of modes obtained from Input/Output (I/O) analysis. Our method applies the linearized Navier–Stokes equations to mean fields and second-order turbulence statistics obtained from ensemble-averages of the experimental data to yield a set of modes across frequencies. Applying a regularized form of Löwdin orthogonalization, we obtain a basis onto which original snapshots can be projected to estimate likely frequencies and corresponding phase-averaged coherent modes in the flow. We apply our method to PIV measurements and corresponding simulations of flow past a spanwise cylinder embedded in a turbulent boundary layer with $\boldsymbol{Re_\tau = 1320}$. While the cylinder sheds regular vortices into its wake, these coherent motions are strongly influenced by the chaotic nature of the background turbulence in the boundary layer. To vary the relative strength of this influence, the experiment and simulations were repeated with cylinders of $\boldsymbol{D/\delta = 0.045}$ and $\mathbf{0.09}$ at a gap width of $\boldsymbol{G/\delta = 0.09}$. In both cases, our method recovers frequencies and coherent flow features, even though the influence of the background turbulence may be quite strong.

## 1 Introduction

Spectral analysis is crucial to understanding a wide variety of fluid flows. Data-driven techniques such as the Fast Fourier Transform (FFT), Dynamic Mode Decomposition

(DMD) [1], and Spectral Proper Orthogonal Decomposition (SPOD) [2] are all useful methods in analyzing dynamics occurring at different frequencies in a flow. One limitation with data-driven spectral analysis, however, is that it requires measurements that are well-resolved in time. Obtaining such data experimentally requires high-speed acquisition rates that may not always be available or feasible. Alternatively, we can perform spectral analysis directly upon the governing equations (e.g., the Navier–Stokes equations). Especially for flow instabilities and their sensitivity to external excitation, linearized versions of the governing equations allow us to solve exactly for spectral features of the flow. Such physics-based spectral analysis techniques include Global Stability Analysis (GSA) [3], Resolvent analysis [4], and Input/Output (I/O) analysis [5, 6]. Importantly, physics-based spectral analysis has no temporal resolution requirement, as it *predicts* a flow's frequency response from the governing equations, given a steady baseflow. For turbulent flows, a relevant steady baseflow might be a time-averaged mean flow measured experimentally, or it might be a numerical solution to the steady Reynolds-Averaged Navier–Stokes (RANS) equations.

While the relative merits of data-driven vs. physics-based techniques can be debated, hybrid methods combining both approaches are particularly powerful tools for understanding flows. A great example of such a synergy is the fact that SPOD modes converge to resolvent response modes in the limit of spatially uncorrelated noise [2]. Conversely, if the SPOD modes do not match the resolvent modes, then the disturbance environment must contain some spatial correlation [7, 8]. Moreover, when this happens, we can use the two analysis methods in tandem to recover the spatial correlation of the disturbance field that must have created the data. In this paper, we take a hybrid approach, and use the relationship between data-driven and physics-based spectral analysis to extract coherent flow dynamics from temporally uncorrelated snapshots. Such a dataset could, for example, correspond to PIV snapshots sampled at a frequency below those relevant to the flow dynamics. Normally, data-driven methods would fail in this case. Individually, however, the PIV snapshots contain a wealth of spatial information, and projecting them onto resolvent response modes allows us to estimate their phase. Our method is similar to conditional projection averaging (CPA) [9] based on resolvent modes, although we use phase averaging to estimate purely harmonic modes. This makes our results comparable to SPOD, and at the same time, allows us to estimate frequency spectra from temporally uncorrelated snapshots.

If a flow is strongly forced periodically at a known rate, then one could simply record the phase of snapshots relative to this known forcing to perform phase averaging. This is similar to recording the instant snapshots are taken using an external clock [10]. For flows with instabilities embedded in turbulence, however, even though the instability may strongly force the flow, the turbulence can provide strong but intermittent perturbations that randomly alter the phase of the instability. Such flows might be best described by a series of intermittent wavepackets with random phase [11]. This randomization prevents clock-based phase-averaging from obtaining useful information above the sampling rate. Alternatively, high-frequency data from point probes (e.g., hot wires or pressure sensors) may be used to estimate the phase of flow features related to the intermittent vortex shedding wavepackets [12–14]. In this

method, the flow provides its own "clock." Hot wire measurements have the potential drawback, however, that they are intrusive and can alter the flow in dynamically sensitive regions. More importantly, the phase estimated from a point probe may be sensitive to its spatial location, and thus placement of the probe may require specific fore-knowledge of the flow dynamics. Beneddine et al. [15] employed resolvent analysis and planar PIV measurements in a turbulent jet flow to demonstrate that the mean velocity field and a time-resolved velocity component at a single point were sufficient to reconstruct the dominant modes corresponding with velocity and pressure variations. They also demonstrated that the location of the single point could impact the accuracy of the results, recommending that the point be located in a zone with strong fluctuations. Similar methods were also employed by Symon et al. [16] to model and analyze time-resolved flow dynamics around an airfoil.

In contrast to these previous strategies, we incorporate spatial information over time-independent planar fields of view to reconstruct energetic spatial modes. Thus, no time-resolved measurements are required. The strategy can be utilized to advantage in future experiments and could also be applied to analyze existing PIV databases that do not include time-resolved signals. Other phase-estimation techniques that incorporate spatial data over a field of view include those based on Proper Orthogonal Decomposition (POD) modes [17]. Such methods have the advantage of being purely data-driven, but ultimately yield modes that are not coherent in time. As explained by Towne et al. [2], SPOD identifies modes that are coherent in both space and time and thus can provide an optimal low-rank representation of space-time covariance statistics. Because resolvent modes are connected to SPOD modes, they also can be used to determine phase. As we will show, resolvent-derived phase averages approximate SPOD modes very well, even though the data used to generate them is not time resolved. Additional phase-estimation techniques using full-field time-resolved data include cyclostationary SPOD (CS-SPOD) [18] and intrinsic phased-based POD (iPhaB POD) [19]. These techniques work best when the flow is nearly perfectly periodic: e.g., vortex shedding from a cylinder in otherwise uniform flow.

In the following, we consider turbulent boundary layer flow past a spanwise-oriented cylinder as an example of a flow containing both coherent and chaotic dynamics. The vortex shedding instability is strongly forced by the chaotic dynamics of the turbulent boundary layer, and while the flow contains some coherence, it is far from perfectly periodic. As discussed below, we repeat the experiment with two different diameter cylinders to alter the relationship between the forcing provided by the background turbulence and the vortex shedding instability in terms of relative strength and frequency. We present a novel method based on orthogonalized I/O modes to estimate both frequency content and phase-averages corresponding to coherent flow dynamics from temporally uncorrelated PIV snapshots, and show that it is effective for both experiments. To compare our method to previous methods relying upon time-resolved information, we augment experimental data with numerical simulations corresponding to the same flow configurations. The remainder of this paper is organized as follows. In Section 2, we discuss our methodology for the experiments, simulations, and I/O analysis and then develop our new method for frequency estimation and phase-averaging. Section 3 then presents results of applying our method to

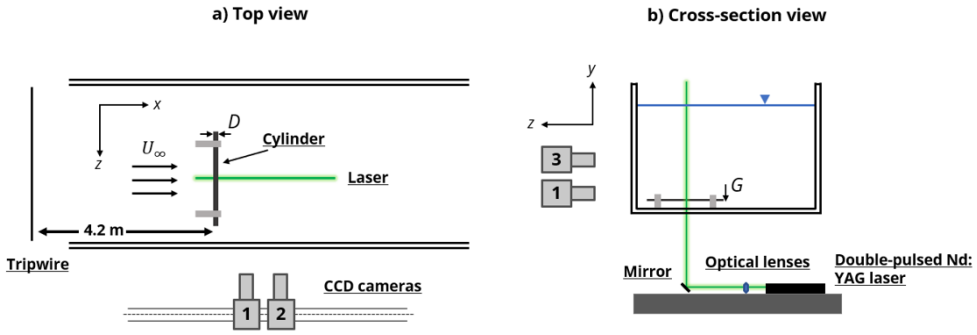



**Fig. 1** Experimental setup. (a) Top view: cylinder and laser sheet position relative to tripwire. (b) Cross-section view: laser path through mirror and sheet optics.

experimental and simulation data. We begin with applying our method to simulation data to compare it to previous methods, and then apply it to experimental data and compare those results to the results obtained from the simulations. Finally, Section 4 discusses the conclusions of the paper.

# 2 Flow configuration and methodology

## 2.1 Experiments

Experiments were performed in a recirculating water channel located in the Turbulent Shear Flow Laboratory in the Aerospace Engineering and Mechanics Department at the University of Minnesota. The channel test section dimensions are 7.80 × 1.12 × 0.58 m. Cylinders were mounted magnetically on the bottom wall a distance 4.2 m downstream of a tripwire located at the test section entrance, as shown in Figure 1. The unperturbed flow speed ($U_\infty = 0.49$ m/s) and conditions ($Re_\tau = 1320$ at the cylinder location) replicate those of previous work completed in the same water channel [20]. Under these conditions, the boundary layer thickness at the streamwise location of the cylinder is $\delta = 69$ mm. In addition to the unperturbed condition, flow measurements were performed for two cylinder diameters $D$, with $D/\delta$ of 0.045 and 0.09 and a fixed gap $G$ between the bottom of the cylinder and the wall such that $G/\delta$ of 0.09. The corresponding cylinder diameters were 6.35 mm (125 viscous units) and 3.175 mm (62 viscous units), and the gap width was 6.35 mm (125 viscous units). For simplification, the cylinders and gap are represented by 'D4', 'D8', and 'G4' respectively (the number indicating inverse distance measured in inches).

Unperturbed flow and flow downstream of each cylinder/gap combination were characterized using planar particle image velocimetry (PIV). For PIV imaging, the flow was seeded with 13 $\mu$m silver-coated hollow glass spheres (Potters Industries LLC), $\rho = 1600$ kg $m^{-3}$. Streamwise/wall-normal image planes were illuminated by two New Wave Solo II Nd:YAG 532 nm lasers controlled by a TSI 610034 synchronizer box. Image pairs were captured with three TSI PowerView Plus 4MPE Cameras (16-bit CCD), positioned as shown in Figure 1. Cameras 1 and 2 were aligned to provide

a relatively long field of view in the streamwise ($x$) direction while Camera 3 was positioned to monitor the outer edge of the boundary layer. Each camera was equipped with a Nikon AF Micro-Nikkor 105mm lens set at f/2.8. The acquisition rate was set at 1 Hz to guarantee statistical independence between fields. A total of 2100 image pairs was captured for each flow condition. Image magnification was 0.05 mm per pixel.

The PIV pre-processing included masking of the raw images and background subtraction to remove wall reflections and enhance contrast. The size of the resulting field of view from Cameras 1 and 2 was $2.3\delta$ in the streamwise direction and $1.2\delta$ in the wall normal direction. Vector fields were computed using DaVis 10.2 from LaVision with a final interrogation window size of 32 by 32 pixels and an overlap of 75%. With this configuration, the vector spacing was approximately 7.5 viscous units.

## 2.2 Numerical Simulations

We use time-resolved, three-dimensional simulations to assess the performance of our new phase averaging method. The simulations solve the incompressible Navier–Stokes and continuity equations,

$$\frac{\partial \mathbf{u}}{\partial t} + (\mathbf{u} \cdot \nabla)\,\mathbf{u} = -\frac{1}{\rho}\nabla p + \nu \nabla^2 \mathbf{u},$$
$$\nabla \cdot \mathbf{u} = 0,$$

where $\mathbf{u}$ and $p$ are the fluid velocity and pressure, respectively. For water, we use a density of $\rho = 1000\,kg/m^3$ and a molecular kinematic viscosity of $\nu = 10^{-6}\,m^2/s$. The equations are solved using a pressure-projection method [21] using finite-differences on a mesh having $512 \times 256 \times 64$ grid points in streamwise, wall-normal and spanwise directions respectively. The computational domain extends $3\delta$ upstream of the cylinder and $2\delta$ downstream. The height and width of the computational domain is $\delta$ in the wall-normal and spanwise directions, respectively. To model the incoming turbulent boundary layer, we apply a digital filtering technique that matches turbulence statistics measured from the water tunnel when no cylinder is present. We apply convective outflow boundary conditions at the downstream outlet and along the top of the domain. A no-slip boundary condition is applied at the wall, and the spanwise direction is treated as periodic. The cylinders are modeled using an immersed boundary method [22]. The simulations are run until all startup transients have left the domain and the flow has settled into a statistically stationary state. After this initial startup period is complete, statistics and snapshots are then collected for further analysis. In the statistics gathering phase, 1000 snapshots were collected at a sample rate of 100 Hz. Each snapshot consisted of the flow velocity on the central $x$-$y$ plane.

The simulations use the simplest possible numerical methods and are underresolved in terms of the scales of turbulence present in the experiment. Nevertheless, as figure 2 shows, the simulations do capture the essential features of vortex shedding from the cylinder and its interaction with turbulence downstream. We expect the subgrid scale motions and gradients present in the experiment but neglected by the simulations to create some discrepancy in the results. The purpose of the simulations, however, is not to match the experiments exactly but rather to provide a means

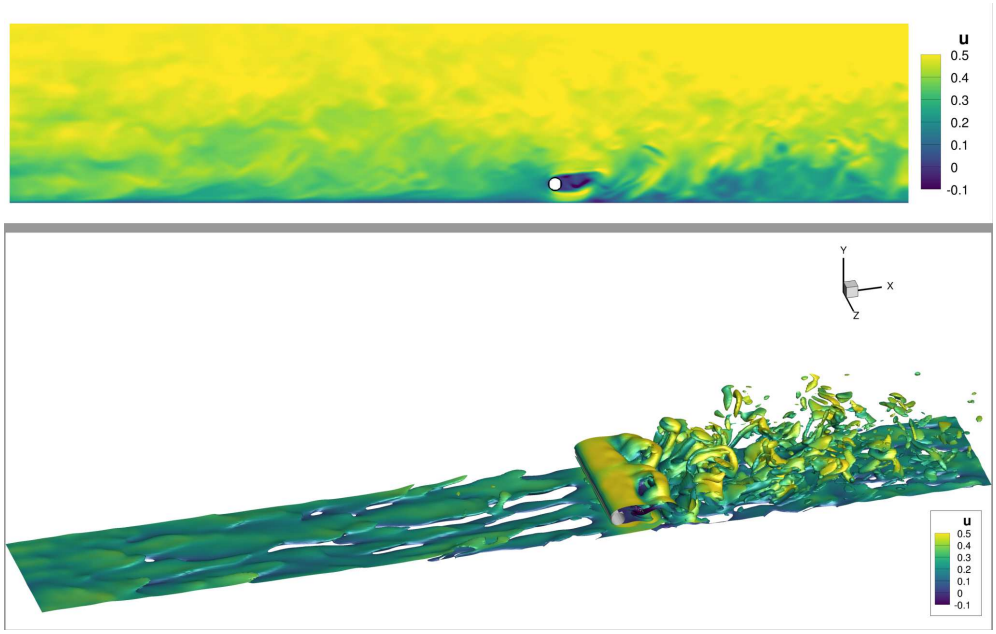



**Fig. 2** D4G4 simulation results. Shown at top are color contours of streamwise velocity on a streamwise slice through the 3D domain. For the same instant in time, the bottom frame shows a 3D isosurface of vorticity magnitude, colored by streamwise velocity.

to evaluate the performance of our phase-averaging methodology relative to SPOD. In this context, any differences are not due to missing subgrid-scale physics. Furthermore, both vortex shedding dynamics and a range of smaller scale motions are well resolved by the simulations.

## 2.3 Resolvent and Input/Output analysis

In the absence of time-resolved measurements, our phase-averaging method instead relies on oscillatory physics embedded in the flow. For boundary layer flow past a cylinder, vortex shedding fulfills this role. In order to exploit it, we first isolate it using resolvent or input/output (I/O) analysis, which are well-known frequency response techniques in the linear systems and controls literature [23]. To apply them, we first consider the linearized Navier–Stokes equations. These equations are formed by decomposing the flow as $\mathbf{u} = \bar{\mathbf{u}} + \mathbf{u}'$ and $p = \bar{p} + p'$, where the overbars and primes denote steady baseflow and perturbation components, respectively. Substituting this decomposition into the Navier–Stokes equations and subtracting the baseflow terms from both sides, yields governing equations for the perturbations,

$$\frac{\partial \mathbf{u}'}{\partial t} + (\bar{\mathbf{u}} \cdot \nabla)\,\mathbf{u}' + (\mathbf{u}' \cdot \nabla)\,\bar{\mathbf{u}} + (\mathbf{u}' \cdot \nabla)\,\mathbf{u}' = -\frac{1}{\rho}\nabla p' + \nu \nabla^2 \mathbf{u}', \tag{1}$$

$$\nabla \cdot \mathbf{u}' = 0, \tag{2}$$

where every term is linear with respect to perturbation quantities, except for $(\mathbf{u}' \cdot \nabla)\,\mathbf{u}'$. Abstractly, we can represent this system as

$$\frac{\partial \mathbf{q}}{\partial t} = A\mathbf{q} + \mathcal{N}(\mathbf{q}), \tag{3}$$

where $\mathbf{q}$ is the perturbation state and $A$ is a time invariant linear operator that depends on the baseflow $\bar{\mathbf{q}}$. The baseflow $\bar{\mathbf{q}} = [\bar{u}\ \bar{v}\ \bar{w}\ \bar{p}]^T$ and perturbation state $\mathbf{q} = [u'\ v'\ w'\ p']^T$ both consist of all components of velocity and pressure. Because the PIV data include only streamwise and wall-normal components, however, we consider only two-dimensional modes with zero spanwise velocity ($\bar{w} = w' = 0$). Furthermore, we neglect $p'$ in the perturbation state because in the pressure-projection method it is completely determined by the perturbation velocity, and acts to enforce the constraint of continuity.

In the limit of small perturbations, $|\mathbf{q}| \ll |\bar{\mathbf{q}}|$, the nonlinear term $\mathcal{N}(\mathbf{q})$ becomes negligible and equation (3) reduces to exactly to the linearized Navier–Stokes equation. Resolvent analysis, however, proceeds by viewing the nonlinear term as a generalized forcing term, $\mathbf{f}$, driving the linearized dynamics,

$$\frac{\partial \mathbf{q}}{\partial t} = A\mathbf{q} + \mathbf{f}. \tag{4}$$

In linearized dynamics, different frequencies do not couple, and we can analyze the flow frequency-by-frequency using the ansatz $\mathbf{f} = \hat{\mathbf{f}} e^{-i\omega t}$, for which the response $\mathbf{q} = \hat{\mathbf{q}} e^{-i\omega t}$ will also be harmonic. The functions $\hat{\mathbf{f}}$ and $\hat{\mathbf{q}}$ are time invariant, and contain the spatial distribution of the forcing and the response functions. This ansatz corresponds to a temporal Fourier transform at angular frequency $\omega$. Solving for $\hat{\mathbf{q}}$,

$$\hat{\mathbf{q}} = (-i\omega I - A)^{-1}\,\hat{\mathbf{f}}. \tag{5}$$

The factor multiplying $\hat{\mathbf{f}}$, which is known as the resolvent operator, represents a transfer function between the forcing $\hat{\mathbf{f}}$ and the response $\hat{\mathbf{q}}$. Applying singular value decomposition to the resolvent operator,

$$(-i\omega I - A)^{-1} = U\Sigma V^*. \tag{6}$$

where $V$ is an orthonormal set of forcing directions linked to a set $U$ of response directions through a set of gains in the diagonal matrix $\Sigma$. The leading singular value gives maximum possible linear amplification at the frequency considered, and the corresponding leading singular vectors of $V$ and $U$ represent the forcing leading to this amplification, and the response resulting from it, respectively. Taken across frequencies, the leading singular vectors form a forcing basis and a corresponding response basis that together represent a reduced-order model of the dominant linearized dynamics.

To determine the true response of the system, however, we need to project the nonlinear term $\mathcal{N}$ onto the forcing basis. One approach is to construct a framework to

account for all possible nonlinear interactions between different frequencies [24, 25]. We instead follow [26] and partly model this term with an eddy viscosity accounting for the interactions between the coherent linearized dynamics and the incoherent motions created by the turbulence [27]. For a cylinder wake in a boundary layer, we use the Boussinesq approximation,

$$\nu_t = \frac{-\langle u'v' \rangle}{\frac{\partial \bar{u}}{\partial y}}, \tag{7}$$

and add the local value of $\nu_t$ to the molecular kinematic viscosity $\nu$. As in an unperturbed boundary layer, the dominant mean velocity gradients are still in the wall normal direction, which provides some justification for the focus on the $\langle u'v' \rangle$ component of the Reynolds stress. More sophisticated eddy viscosity models [28] might be needed for more complicated flows. For our configuration, however, we find the above model to be sufficient.

As a damping term, eddy viscosity is important to the downstream development of wavepackets in resolvent analysis. To initiate the wavepackets, however, we find that it is also necessary to weight the input forcing based on the local intensity of turbulence in the flow. We do this using an operator $B$,

$$\frac{\partial \mathbf{q}}{\partial t} = A\mathbf{q} + B\mathbf{f}. \tag{8}$$

Here, we assume $B$ is a simple diagonal operator proportional to the two-component turbulent kinetic energy (TKE),

$$k = \frac{1}{2}\left\langle u'^2 + v'^2 \right\rangle, \tag{9}$$

where $w'$ is not included because it is not available in the PIV measurements. Even though we treat the term $\mathcal{N}$ as stochastic forcing, it should be proportional to the local TKE in the Navier–Stokes equations owing to their quadratic nonlinearity. The forcing is much more likely to be strong in regions of high TKE than it is away from the turbulence, so we weight the stochastic forcing accordingly. Similar to the eddy viscosity, we use the snapshots from the perturbed turbulent boundary layers to calculate the TKE weighting field. Weighting the forcing and potentially the response are key components of input/output (I/O) analysis that differentiate it from resolvent analysis. We therefore call the modes we obtain in the remainder of this paper "I/O modes."

## 2.4 Projection onto I/O modes and phase averaging

For time-resolved data, a phase-average can be obtained from a sequence of snapshots $\mathbf{q}(\mathbf{x}, t)$ by averaging together snapshots offset by a time-delay, $T$. Equivalently, we can consider the Fourier transform

$$\hat{\mathbf{q}}(\mathbf{x}, \omega) = \int_0^{T_f} \mathbf{q}(\mathbf{x}, t) e^{-i\omega t} dt, \tag{10}$$

for a given angular frequency $\omega = 2\pi/T$. While $T_f$ may correspond to the entire duration of the snapshot sequence, a better signal-to-noise ratio may be obtained by computing an average from an ensemble of $\hat{\mathbf{q}}$'s over shorter subsequences of the data (i.e. Welch's method [29]). Spectral Proper Orthogonal Decomposition (SPOD) extends this idea by applying singular value decomposition to the ensemble of $\hat{\mathbf{q}}$'s instead. Both the FFT and SPOD require uniform sampling in time, and are limited by the Nyquist frequency $\pi/\Delta t$, where $\Delta t$ is the time between snapshots.

For non-time-resolved data, computing the Fourier transform in the usual way is not possible. If, however, the phase $\phi = \omega t$ can be estimated from each snapshot independently, then we can evaluate the Fourier integral stochastically as

$$\hat{\mathbf{q}}(\mathbf{x},\omega) = \int \mathbf{q}(\mathbf{x},t)e^{-i\omega t}dt \approx \left\langle \mathbf{q}_j e^{-i\phi} \right\rangle, \tag{11}$$

where $\mathbf{q}_j = q(x,t_j)$ represents the $j$th snapshot, and the angle brackets represent ensemble averaging. To estimate the phase for a given frequency $\omega_k$, we first project each snapshot onto the I/O mode at that frequency using the inner product,

$$c_{j,k} = \int \mathbf{q}_j \mathbf{u}_k^* \, d\mathbf{x}. \tag{12}$$

Here, $c_{j,k}$ is the projection coefficient of the $j$th snapshot onto the I/O mode at the $k$th frequency. In (12), $\mathbf{u}_k$ denotes the I/O mode at frequency $\omega_k$ (the first column of $U$ from (6), and $\mathbf{u}_k^*$ is its complex conjugate. The resulting complex projection coefficient $c_{j,k} = |c_{j,k}|e^{i\phi_{j,k}}$ can then be written in terms of its magnitude $|c_{j,k}|$ and phase $\phi_{j,k}$. We then use $\phi_{j,k}$ to perform phase-averaging,

$$\hat{\mathbf{q}}_k = \left\langle \mathbf{q}_j e^{-i\phi_{j,k}} \right\rangle, \tag{13}$$

where $\hat{\mathbf{q}}_k = \hat{\mathbf{q}}(\mathbf{x},\omega_k)$ and the angle brackets correspond to averaging over snapshots. It is worth noting that the projection (12) and the method of determining $\phi_{j,k}$ is the same as that of Conditional Projection Averaging (CPA) [9]. While CPA used phase-binning to construct modes associated with a known dominant frequency, we seek harmonic modes $\hat{q}_k$ by estimating the Fourier transform. As we will see, the Fourier transform method allows capture of modes over a broad range of frequencies.

While phase-averaging using $\phi_{j,k}$ leads to estimates of Fourier modes $\hat{\mathbf{q}}_k$, we would like to use the amplitudes $|c_{j,k}|$ from projection (12) to estimate frequency spectra, too. For time-resolved data, frequency spectra are computed by applying a Fourier transform to temporal data taken at single points in the flow. Because the Fourier transform projects temporal data onto an orthogonal basis of sine and cosine functions, it partitions the data's variance exactly among frequencies (Parseval's theorem). For temporally uncorrelated snapshots, however, a simple temporal basis of sines and cosines is not available and we must rely upon the projection (12) to fill this role. While the I/O modes provide a good physical basis for this purpose, they are not orthogonal, as modes at nearby frequencies tend to resemble each other. In this case,

**Algorithm 1** I/O projection averaging

Inputs: $Q_{N\times N_j}$, $U_{N\times N_k}$, $\gamma$
$G' = U^*U + \gamma I$ ▷ Modified Gramian
$G' \rightarrow T\Lambda T^*$ ▷ Eigendecomposition
$U' = UT\Lambda^{-1/2}T^*$ ▷ Löwdin orthogonalization
**for** $k = 1, ..., N_k$ **do**
  $PSD_k = 0$ ▷ Power spectral density
  $\hat{Q}_{:,k} = 0_{N\times 1}$
  **for** $j = 1, ..., N_j$ **do**
    $c_{k,j} = \int U'^*_{:,k} Q_{:,j} d\mathbf{x}$ ▷ Projection coefficient
    $PSD_k \leftarrow PSD_k + |C_{k,j}|^2$
    $\hat{Q}_{:,k} \leftarrow \hat{Q}_{:,k} + Q_{:,j} e^{-i \arg(C_{k,j})}$
  **end for**
  $a_k \leftarrow \sqrt{\frac{PSD_k}{N_j}}$ ▷ Amplitude at frequency $k$
  $\hat{Q}_{:,k} \leftarrow \frac{\hat{Q}_{:,k}}{N_j}$ ▷ Phase average at frequency $k$
**end for**

the variance in the original dataset is not perfectly partitioned among frequencies by the projection.

If we collect the I/O modes as columns of a matrix $U$, however, it is possible to find the "closest" orthogonal matrix $U'$ (for which $||U - U'||_F$ is minimized) using Löwdin orthogonalization [30],

$$U' = UT\Lambda^{-1/2}T^*. \tag{14}$$

Here, $\Lambda$ and $T$ are Hankel eigenvalues and eigenfunctions of the Gramian $G = U^*U$. $G$ is a frequency domain approximation of the controllability Gramian [31, 32]. $UT\Lambda^{-1/2}$ are the Empirical Orthogonal Functions (EOFs) that represent responses most easily excited by input forcing across all frequencies [33, 34]. EOFs also correspond to Löwdin's canonical orthogonalization for highly oblique bases where $U$ is low-rank, which is often the case for flows supporting instabilities. In this case, while multiplying the EOFs by $T^*$ produces an orthogonal basis, the basis vectors are sensitive to noise, especially in spatial regions away from the instability where the original I/O modes contain little content. To ameliorate this situation, we consider eigenvalues and eigenfunctions of the modified Gramian,

$$G' = U^*U + \gamma I, \tag{15}$$

where $\gamma \ll 1$. As $\gamma$ increases from zero, we relax the condition that $U'$ remain strictly orthogonal, but we reduce sensitivity of the basis vectors to noise. As $\gamma \rightarrow \infty$, $G'$ becomes increasingly diagonal and we recover the original basis vectors as $U' \rightarrow U$.

Algorithm 1 gives a step-by-step description of our frequency estimation and phase averaging procedure. As input, our method takes an $N \times N_j$ snapshot matrix $Q$, the columns of which are the statistically independent snapshots of our flow state

**q**. $U$ is an $N \times N_k$ input matrix of I/O modes calculated from the singular value decomposition, and a relaxation parameter $\gamma$. Here, $N$ is the number of data points per snapshot. For the current study, this is twice the number of grid points, as each snapshot includes both the $u$ and $v$ components of velocity. $N_j$ and $N_k$ are the number of snapshots and the number of frequencies considered, respectively. In lines 2-4, we use a regularized form of Löwdin orthogonalization to construct an orthogonal or nearly-orthogonal basis that remains close to the original basis of I/O modes across frequencies. This allows us to incorporate both amplitude and phase information when we project an ensemble of snapshots to estimate both the frequency and modal content of the flow dynamics that produced them, in lines 5-15. The constraint of remaining close to the original basis of I/O modes also differentiates our method from EOFs which span the same subspace but which mix information at different frequencies. The introduction of the relaxation parameter $\gamma$ allows us to consider a smooth range of different projection bases, from perfectly orthogonal when $\gamma = 0$ to the original non-orthogonal basis of I/O modes as $\gamma \to \infty$. Ideally, $\gamma = 0$ so that $U'$ is perfectly orthogonal and Parseval's theorem is satisfied exactly. Practically, though, we find that the introduction of very small values of $\gamma$ greatly reduces the sensitivity of the method to noise, while maintaining a high level of accuracy. Finally, we note our I/O projection averaging algorithm is quite computationally efficient. For example, note that $G'$ has dimensions $N_k \times N_k$, which for the current study was $80 \times 80$, so the eigendecomposition can be accomplished in a fraction of a second on modern computers.

# 3 Results

In the following subsections, we first compare time-averaged baseflows from the simulations and experiments. Then, we evaluate the spectral content in the simulations using traditional methods that rely on time-resolved data. At the same time, we compute I/O modes that predict this spectral content from the time-averaged baseflows. Next, we apply our new frequency-estimation and phase-averaging method to the snapshots from the simulation, to show that it recovers the same results as the traditional methods. Finally, we apply our new method to temporally uncorrelated PIV snapshots from the experiments.

## 3.1 Time-averaged statistics

Figure 3 compares mean fields from the simulation and experiments for the D4G4 case: the larger of the two cylinders. Figures 3 (a) and (b) show contours of the mean streamwise velocity, normalized by the freestream velocity ($\bar{u}/U_\infty$). Although the domain for the simulation extends far upstream, we consider only the region beginning just downstream of the cylinder corresponding to the PIV field of view. In both the simulation and experiment, we observe the flow to accelerate above and below the cylinder and a wake to form immediately behind the cylinder. The flow acceleration underneath the cylinder causes a wall jet to form in the gap between the wall and cylinder. These effects are stronger in the simulation than in the experiment, although the flow is qualitatively similar. Another important difference is that the simulation exhibits mean reversed flow in the cylinder wake whereas the experimental mean flow

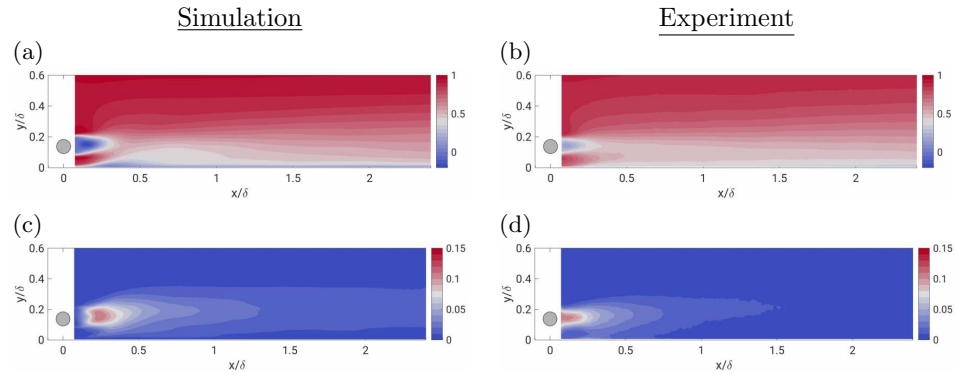



**Fig. 3** Time-averaged flow fields from the simulation (a and c) and from the experiment (b and d) for the D4G4 configuration. Panels a and b show color contours of mean non-dimensional streamwise velocity, $\bar{u}/U_\infty$, while panels c and d show color contours of the two-component non-dimensional turbulent kinetic energy $k/U_\infty^2$.

does not. We attribute these differences to the broader range of scales of turbulence present in the experiment as compared to the simulation, which enhance momentum diffusion.

Figures 3(b) and (d) show contours of non-dimensional turbulent kinetic energy $k/U_\infty^2$ for the simulation and experiment. The peak TKE occurs in the wake behind the cylinder, and the levels are approximately the same in the simulation and experiment. The peak TKE in the simulation occurs a bit further downstream than it does in the experiment. This difference can again be explained by the missing scales of turbulence in the simulation.

Figure 4 shows the same fields as Figure 3, but for the D8G4 (smaller cylinder) flow configuration. Again, we find that the simulation captures the essential features of the experiment, although the wake is stronger and the TKE peak is offset downstream in the simulation compared to the experiment. These differences are similar to those observed in the D4G4 case.

## 3.2 Spectral content

To analyze the spectral content in the simulations, we first apply SPOD to snapshots relatively closely spaced in time. The snapshots are comprised of instantaneous mean-subtracted fluctuating velocity components on a single two-dimensional ($x$-$y$) plane cutting through the 3D simulation domain. The plane's position was chosen to match the field-of-view of the PIV, extending from just behind the cylinder to about $2.4\delta$ downstream. The plane also extended to $1.2\delta$ in the wall-normal direction, although the vortex shedding modes are mostly concentrated in the lower half of the domain. To match the PIV, we also use only the streamwise and wall-normal components of the fluctuating velocity in the SPOD calculations. For vortex shedding, we non-dimensionalize frequency using a Strouhal number based on the cylinder diameter $D$ and mean velocity $U_c$ at position of the cylinder's center in the unperturbed boundary layer. For a fixed gap width, note that the center of the cylinder in the D4G4 configuration is slightly farther from the wall than in the D8G4 case. Therefore, $U_c = 0.3449$

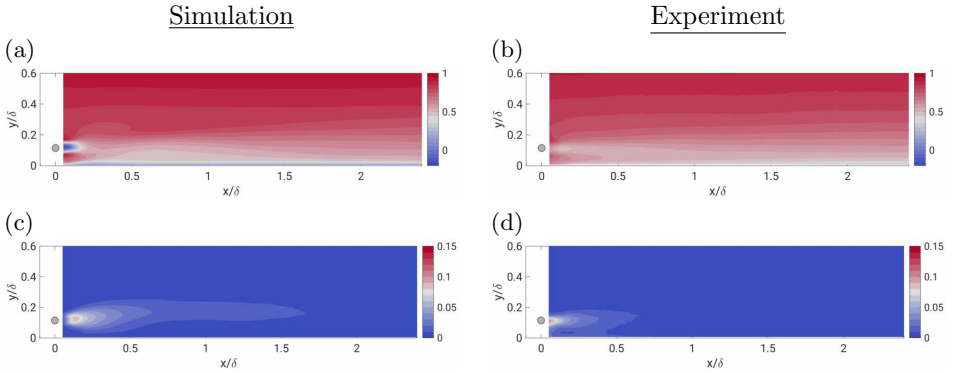



**Fig. 4** Time-averaged flow fields from the simulation (a and c) and from the experiment (b and d) for the D8G4 configuration. Panels a and b show color contours of mean non-dimensional streamwise velocity, $\bar{u}/U_\infty$, while panels c and d show color contours of the two-component non-dimensional turbulent kinetic energy $k/U_\infty^2$.

m/s for D4G4 while $U_c = 0.3356$ m/s for D8G4. The 100 Hz sampling rate in the simulations corresponds to $St_{samp} = 1.84$ for D4G4 and $St_{samp} = 0.95$ for D8G4. In both simulations, 1000 snapshots were recorded, and SPOD was performed using a window size of 200 with a 50% overlap. Each snapshot included both the streamwise and wall-normal components of the fluctuating velocity.

Figure 5 shows spectra of the first 5 SPOD modes for the D4G4 and the D8G4 simulations. The spectra of the leading SPOD mode in both simulations contain a strong peak near $St = 0.2$ similar to vortex shedding frequencies downstream of cylinders in uniform flow [35]. For D4G4, this peak occurs at $St_{shed} = 0.21$, while for D8G4 it occurs at $St_{shed} = 0.17$. The lower frequency in the D8G4 case (similar to lower frequencies observed for $Re_D < 400$ in uniform flows [36]) might be explained by under-resolution of the boundary layer that forms over the cylinder. The spectra of the leading SPOD modes contain additional peaks at the sub-harmonic and first harmonic frequencies (see black dots in Figure 5).

Figures 6 and 7 compare SPOD modes to I/O response modes ($\mathbf{u}_k$) at the same three frequencies for both flow cases. The I/O modes were computed using ensemble-averaged baseflows and TKE fields from the simulations. For purposes of comparison, all modes (both SPOD and I/O) were scaled to have unit $\ell_2$-norm. As the figures show, the I/O mode shapes agree well with the SPOD mode shapes. For the D4G4 simulation, the correlation between the SPOD mode and I/O mode at the fundamental frequency (panels c and d in Figure 6) was 0.93. The SPOD–I/O mode correlations for the sub-harmonic and first-harmonic were 0.55 and 0.48, respectively. The high correlation value at the fundamental frequency suggests that the strong vortex shedding dominates the dynamics. The D8G4 simulation shows greater differences between SPOD and I/O modes, although the mode correlations are still high (0.67 for the modes at the fundamental frequency and 0.56 and 0.53 for the sub-harmonic and first harmonic frequencies respectively) suggesting that the vortex shedding is less dominant in this case.

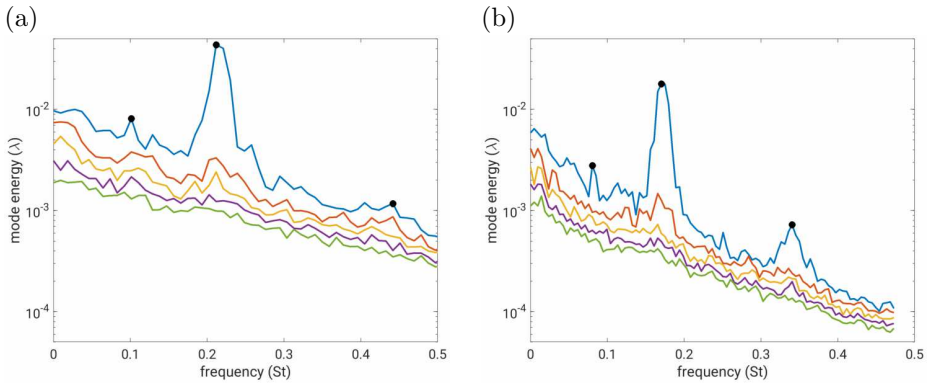



**Fig. 5** SPOD spectra for two-component velocity fields in the (a) D4G4 and (b) D8G4 simulations. Spectra corresponding to the five leading modes are shown. The leading mode spectrum shows a strong peak at the fundamental vortex shedding frequency in both simulations, as well as peaks at sub-harmonic and first harmonic frequencies (marked with black dots).

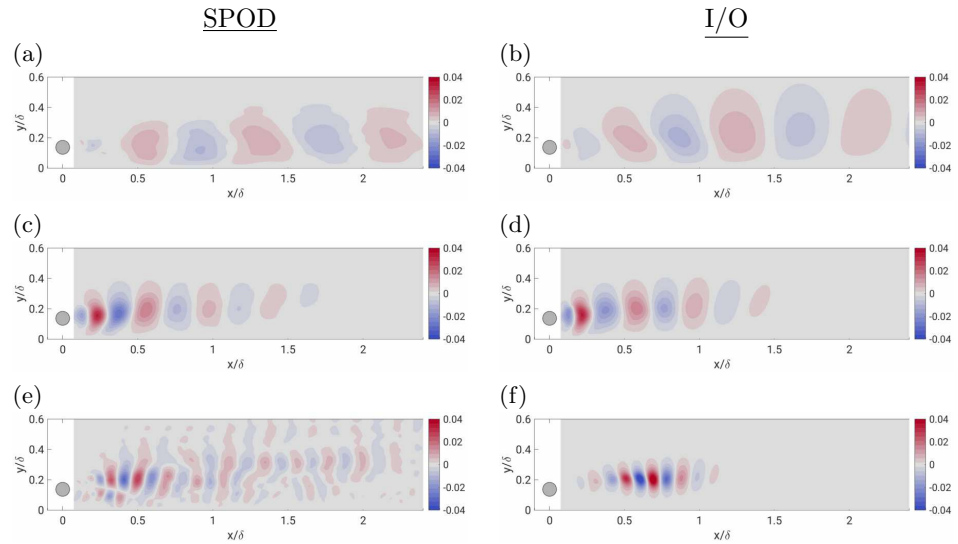



**Fig. 6** SPOD modes (left column, a–c) and I/O modes (right column, b–f) for the D4G4 simulation at the three frequencies marked by black dots in Figure 5(a). From top to bottom, these frequencies are the subharmonic $St = 0.10$ (panels a and b), the vortex-shedding fundamental frequency $St = 0.21$ (panels c and d), and the first harmonic $St = 0.44$ (panels e and f). Color contours of the wall-normal velocity fluctuation are shown.

## 3.3 Frequency estimation and phase averaging

Figure 8 shows estimated spectra for the D4G4 and D8G4 simulations obtained by projecting onto bases $U'$ with different values of $\gamma$ as explained in Section 2.4. We obtain these spectra by averaging $|c_{k,j}|$ over all simulation snapshots for each frequency. When $\gamma = 0$, the spectra are somewhat noisy, although each shows a clear peak at the vortex shedding frequency ($St_{shed} = 0.21$ for D4G4 and $St_{shed} = 0.17$ for

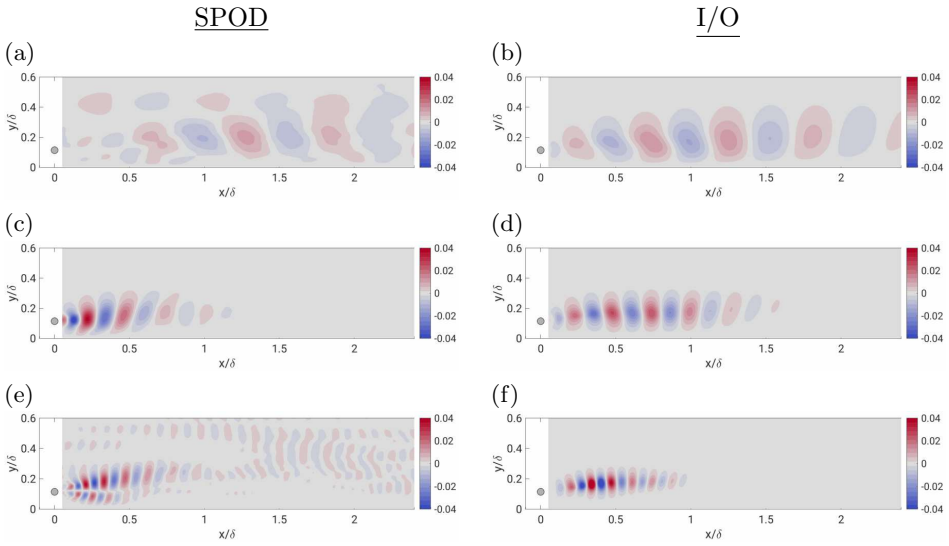



**Fig. 7** SPOD modes (left column, a–c) and I/O modes (right column, b–f) for the D8G4 simulation at the three frequencies marked by black dots in Figure 5(b). From top to bottom, these frequencies are the subharmonic $St = 0.08$ (panels a and b), the vortex-shedding fundamental frequency $St = 0.17$ (panels c and d), and the first harmonic $St = 0.34$ (panels e and f). Color contours of the wall-normal velocity fluctuation are shown.

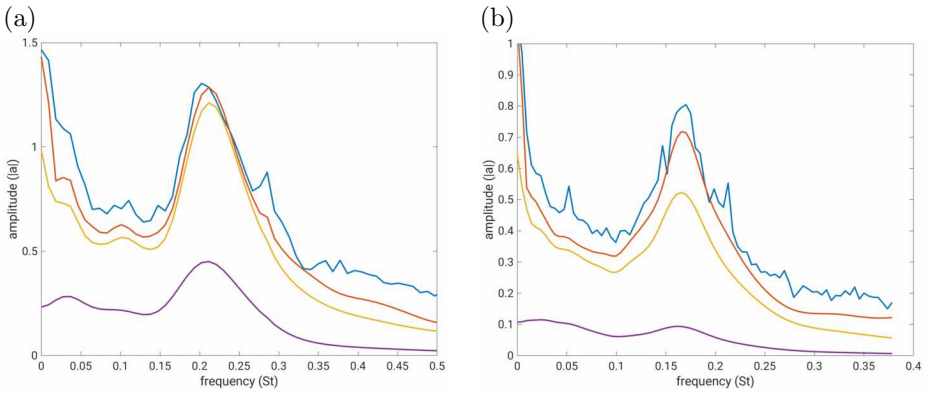



**Fig. 8** Frequency spectra estimated by projecting two-component velocity field snapshots from the (a) D4G4 and (b) D8G4 simulation onto bases of orthogonalized I/O modes. In each plot, the blue, red, yellow, and purple lines correspond to $\gamma = 0$, $10^{-8}$, $10^{-6}$, and $10^{-4}$, respectively.

D8G4, from figure 5). Even a small $\gamma$, e.g. $\gamma = 10^{-8}$, is enough to significantly smooth the spectra, and reveal another peak at the sub-harmonic frequency in the case of D4G4. As $\gamma$ increases, the I/O modes begin to overlap significantly and the projection performance deteriorates. Finally, even though the simulation snapshots were time-resolved, no temporal information (except that encoded by the I/O modes) was used to estimate these spectra.

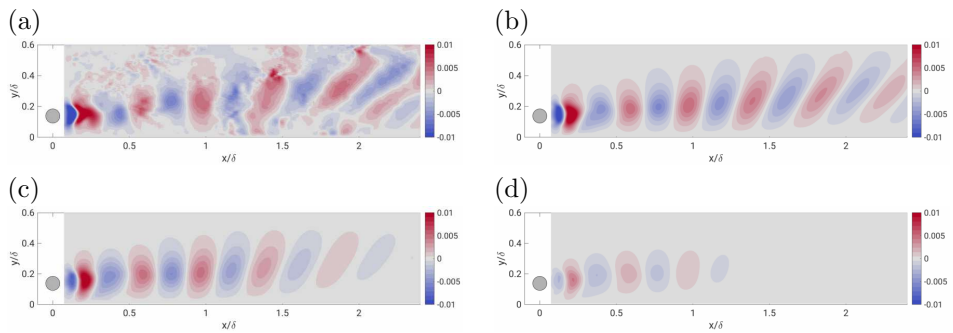



**Fig. 9** The effect of $\gamma$ on the orthogonalized basis function ($U'$) at $St = 0.21$ for the D4G4 simulation. Here the panels correspond to (a) $\gamma = 0$, (b) $\gamma = 10^{-8}$, (c) $\gamma = 10^{-6}$, and (d) $\gamma = 10^{-4}$. When $\gamma = 0$ the basis function is perfectly orthogonal to basis functions at nearby frequencies, whereas for $\gamma = 10^{-4}$, the basis function closely resembles the original I/O mode.

Figure 9 shows the orthogonalized I/O mode at the fundamental frequency ($St = 0.21$) for the D4G4 simulation. When $\gamma = 0$, we can see that the mode is sensitive to noise especially in regions away from the cylinder wake where the original I/O modes had minimal content. Introduction of a non-zero $\gamma$ removes much of this noise while maintaining the shape and magnitude of the mode shapes, and as $\gamma$ increases, the shapes grow increasingly similar to the original I/O mode (see Figure 6(d)).

While the amplitudes $|c_{k,j}|$ of the complex projection coefficients are useful to estimate the spectral content of a flow from a set of snapshots, we can use the phases $\phi_{k,j}$ to perform phase averaging. Figure 10 shows phase-averaged modes at the fundamental, sub-harmonic and first harmonic vortex shedding frequencies for the D4G4 simulation. At the fundamental frequency ($St = 0.21$, middle row), the phase averaged mode is quite similar in structure to the I/O mode at the same frequency. This is expected, as the dynamics at the frequency are quite low-rank (there is a large difference in mode energy between the first two SPOD modes at this frequency). The phase averaged mode at the sub-harmonic frequency ($St = 0.10$, top row) appears to have a long wavelength component downstream (similar to the I/O mode at that frequency) and a shorter wavelength component upstream. The shorter wavelength approximately matches the wavelength of the phase-averaged mode at the fundamental frequency. Because this phase average is formed over an ensemble of snapshots, we interpret the short-wavelength section to be a result of the specific arrangement of upstream vortices needed to precipitate vortex pairing corresponding to the phase observed downstream. At the first harmonic frequency ($St = 0.44$, bottom row), even though there is no obvious peak in the spectrum, phase averaging reveals that organization still exists, and persists downstream of the cylinder at least one boundary layer thickness.

The two columns of Figure 10 compare phase averaging using two different bases calculated using the two extreme values $\gamma = 0$ and $\gamma = 10^{-4}$ for the D4G4 simulation. Unlike the frequency estimation, this figure shows that the phase-averaging is rather insensitive to the exact details of the orthogonalization. The largest differences appear to occur at high frequency, as seen by comparing Figures 10(e) and (f). We believe the

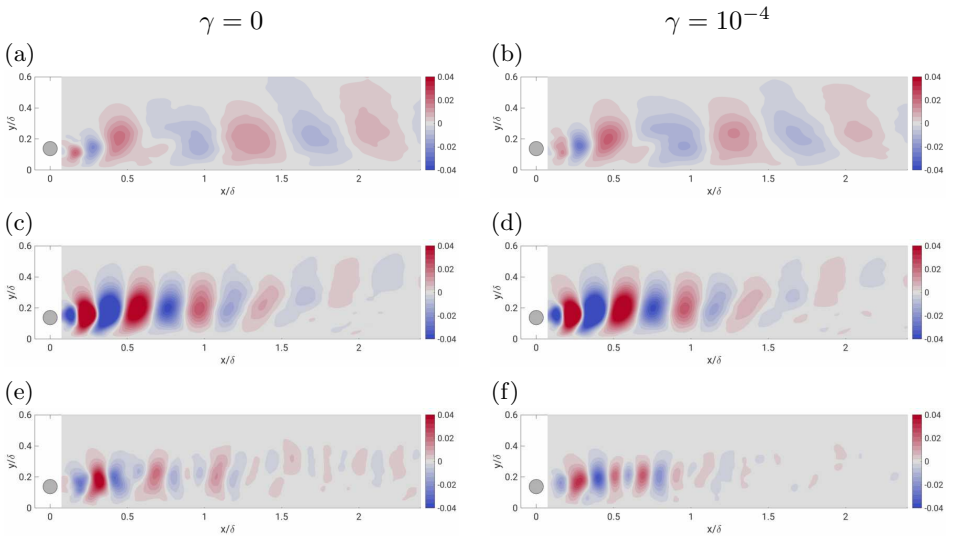



**Fig. 10** Phase-averaging at (a and b) St = 0.10, (c and d) St = 0.21, and (e and f) St = 0.44 for the D4G4 simulation. In the first column (a–e) phase averaging was performed using a perfectly orthogonal basis with $\gamma = 0$, whereas in the second column phase averaging was performed using a basis closely resembling the original I/O modes with $\gamma = 10^{-4}$. Color contours of wall-normal velocity are shown.

insensitivity of the phase averaging occurs because the basis functions are all similar in the near-wake region just downstream of the cylinder, irrespective of the value of $\gamma$ (see Figure 9). This suggests that the near-wake region is the most important in determining the phase in this flow, which makes sense because this is the location where vortex shedding is felt most keenly by the flow. In this sense, the basis provided by the original I/O modes ($U$ in equation 14) may be sufficient for the purposes of phase averaging. The frequencies that vortex shedding imparts to the flow, on the other hand, do persist farther downstream, even though they may become disordered in terms of phase. Compared to the original basis, the orthogonalized functions used for the frequency spectrum estimation thus extend farther downstream to recover this energy.

Finally to further assess the influence of $\gamma$, we consider projections of an individual snapshot $q$ onto the subspaces spanned by bases of orthogonalized I/O modes. If $U'$ is the basis after performing regularized Löwdin orthogonalization for a given $\gamma$, then the projection $\tilde{q}$ can be obtained as

$$\tilde{q} = U'U'^{*}q. \tag{16}$$

Figure 11 shows a typical snapshot of the perturbation velocity components taken from the D4G4 simulation alongside several projections onto bases obtained using different $\gamma$'s. All of the projections reveal the presence of a strong vortex shedding mode immediately downstream of the cylinder until $x/\delta \approx 0.75$. This mode appears especially strong in the wall-normal velocity fields, although it is also evident in the streamwise velocity fields. For $x/\delta > 0.75$, the projections show a weaker mode with

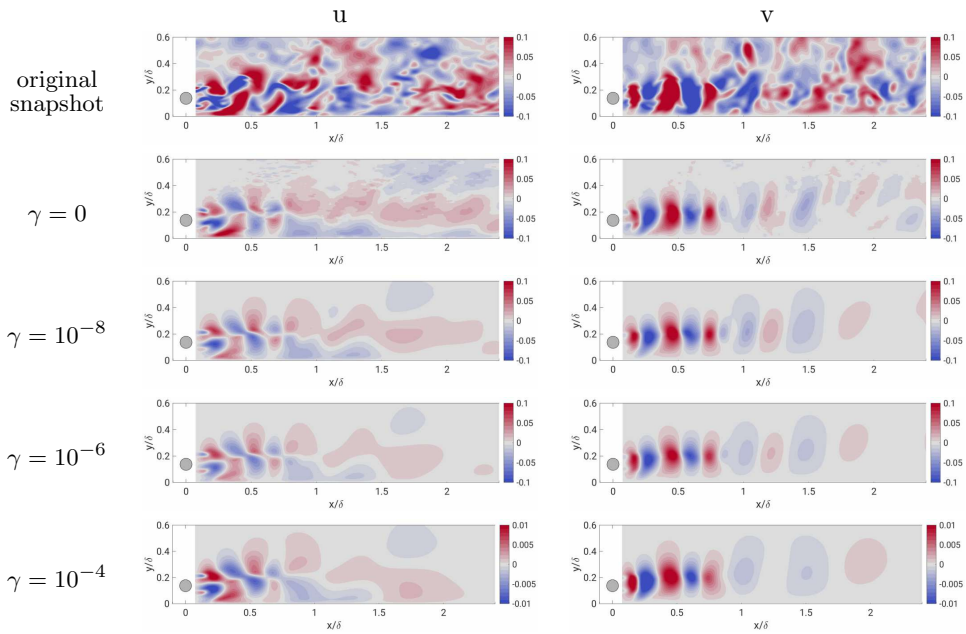



**Fig. 11** Projection of a single snapshot (top row) from the D4G4 simulation after projection onto bases of orthogonalized I/O modes. Color contours of streamwise (left column) wall-normal (right column) velocity perturbation are shown. The second row corresponds to projection on a perfectly orthogonal basis, while the others show the effect of increasing the relaxation parameter $\gamma$.

wavelength approximately double that of the vortex shedding mode. We interpret this downstream mode to be the consequence of vortex pairing.

When $\gamma = 0$, the projection basis is perfectly orthogonal across all frequencies, but the basis vectors are sensitive to noise, as the second row of Figure 11 shows. In this case, the projection actually captures some of the fine scale turbulence along with the vortex shedding. As $\gamma$ increases, the projections become progressively smoother, and also tend to focus more on the region of primary vortex shedding rather than the vortex pairing downstream. When at the larger $\gamma = 10^{-4}$, the amplitude of the projection reduces significantly (note the different color scale and the loss of the red structure near $x/\delta \approx 1.25$), an effect also apparent in Figure 8. In other words, as $\gamma$ increases, the projections become smoother but they also capture fewer features of the original snapshot. This effect initially helps to extract the coherent motions within the flow by filtering out the fine scale turbulence. While the coherent vortex shedding mode is readily apparent in the original snapshot, the coherence of the downstream vortex pairing is somewhat obscured by the the fine scale turbulence. Projection with $\gamma = 0$, reveals the presence of the downstream pairing mode (and highlights it in the original snapshot, when view side-by-side). The pairing mode becomes even more clear when $\gamma = 10^{-8}$. As $\gamma$ increases further, however, the pairing mode is gradually lost in favor of the primary vortex shedding mode.

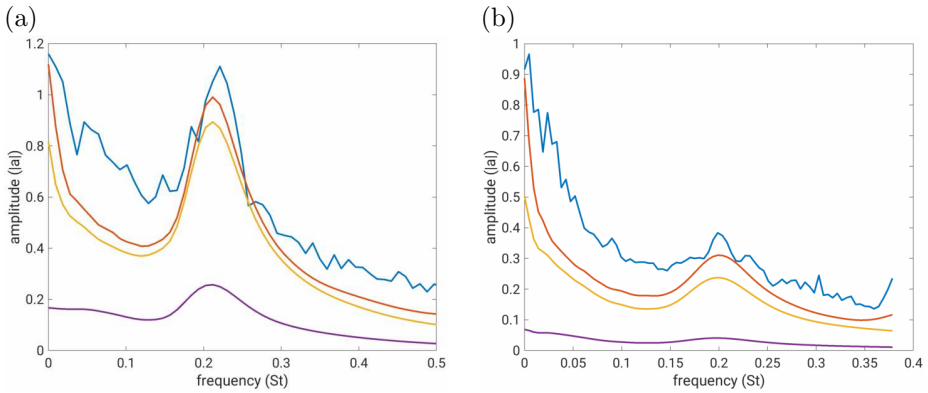



**Fig. 12** Frequency spectra estimated by projecting two-component velocity field snapshots from the (a) D4G4 and (b) D8G4 experiments onto bases of orthogonalized I/O modes. In each plot, the blue, red, yellow, and purple lines correspond to $\gamma = 0$, $10^{-8}$, $10^{-6}$, and $10^{-4}$, respectively.

## 3.4 Experiments

We now apply our methodology to analyze non-temporally-correlated PIV snapshots acquired in the D4G4 and D8G4 experiments. As discussed previously, the experiments had a greater range of turbulent scales than the simulations. In the experiments, this caused a weaker ensemble-averaged wake, as fine scale turbulence tends to enhance diffusion (see Figures 3 and 4).

Because the PIV snapshots are not time-resolved, we cannot obtain a frequency spectrum using SPOD. Instead, we apply the frequency estimation technique described in Section 2.4, via projection onto orthogonalized I/O modes. Figure 12 shows the results for the D4G4 and D8G4 PIV datasets. For the D4G4 experiment, the estimated frequency spectrum shown in Figure 12(a) is remarkably similar to the spectrum shown in Figure 8(a) obtained from the D4G4 simulation. The experimental spectrum shows a strong peak at the vortex shedding frequency $St_{shed} = 0.21$ in perfect agreement with the vortex shedding frequency in the simulation. Different from the simulation, the experimental spectra do not show distinct peaks at the sub-harmonic or first harmonic frequencies. Similar to the D4G4 case, the D8G4 experimental spectrum shows a peak at the fundamental vortex shedding frequency, although this peak is weaker than the vortex shedding peak in D8G4 simulation (see Figure 8(b)). In the experiment, this peak occurs at a higher frequency ($St_{shed} = 0.20$) than in the simulation (where $St_{shed} = 0.17$). The lesser amplitude of the vortex shedding in the D8G4 experiment is consistent with a weaker wake compared to simulation, while the higher shedding frequency matches what is expected based on the literature.

Figure 13 shows the I/O modes at the fundamental and sub-harmonic frequencies computed using the ensemble-averaged baseflows from the D4G4 and the D8G4 experiments. The eddy viscosity and TKE fields used by the I/O analysis were computed from ensemble averages of the PIV fields. Similar to those derived from the simulations, I/O modes about the experimental baseflow take the form of wavepackets in the wake behind the cylinders. The modes corresponding to the experimental data in Figure 13 are remarkably similar to the modes corresponding to the simulations in

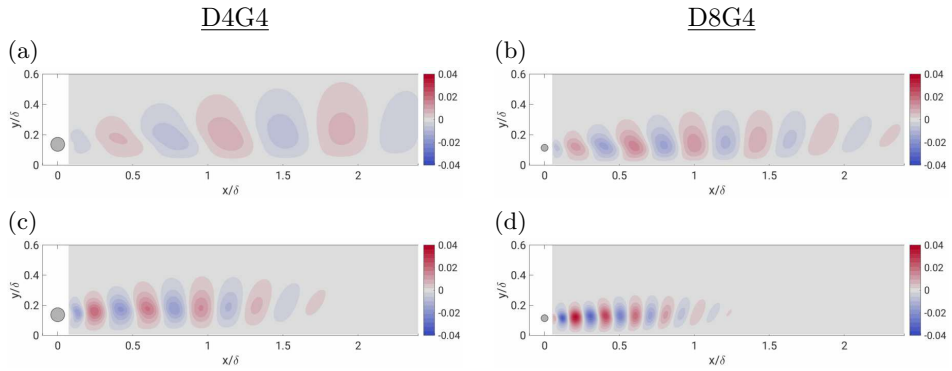



**Fig. 13** I/O modes corresponding to the (a and c) D4G4 and (b and d) D8G4 experiments. Color contours of wall-normal velocity perturbation are shown. The first row (a and b) shows I/O modes at the sub-harmonic frequency ($St = 0.1$) while the second row (c and d) shows I/O modes at the fundamental vortex shedding frequency ($St = 0.2$).

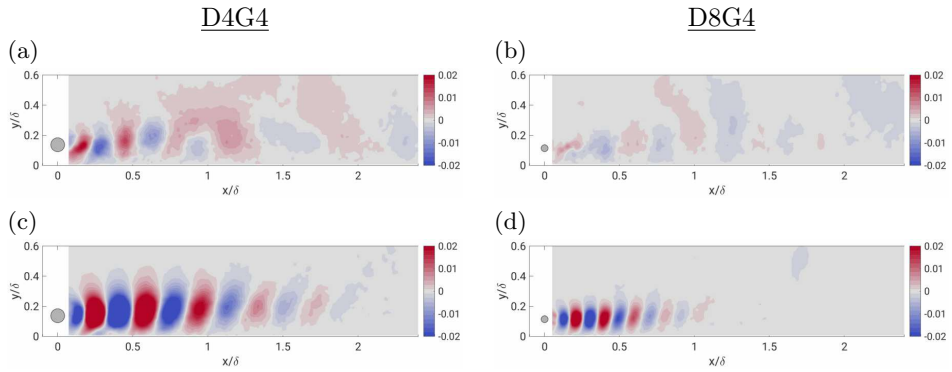



**Fig. 14** Phase averaging using projection onto orthogonalized I/O modes for the (a and c) D4G4 and the (b and d) D8G4 experiments. Similar to Figure 13, the first row (a and b) corresponds to the sub-harmonic frequency ($St = 0.1$) while the second row (c and d) corresponds to the fundamental vortex shedding frequency ($St = 0.2$). Color contours of wall-normal velocity perturbation are shown.

Figures 6 and 7. In both cases, high frequency, short wavelength modes tend to die out more quickly downstream than their lower frequency counterparts.

As was demonstrated with the simulations, we next apply phase averaging to the PIV snapshots to extract spatially coherent features from the data. Figure 14 shows the results of phase averaging at the fundamental and sub-harmonic frequencies for both PIV datasets. Similar to the simulations, phase averaging at the fundamental frequency (panels (c) and (d) in Figure 14) yielded modes quite similar to the I/O modes at the same frequency (compare these to Figures 13(c) and (d)). At the sub-harmonic frequencies, phase averaging of the PIV snapshots yields an upstream section of a short wavelength mode followed by a downstream section containing a long wavelength mode. This structure is much less clear, however, than it was for the simulation data, in keeping with the absence of the sub-harmonic peak in the experimental estimated spectra.

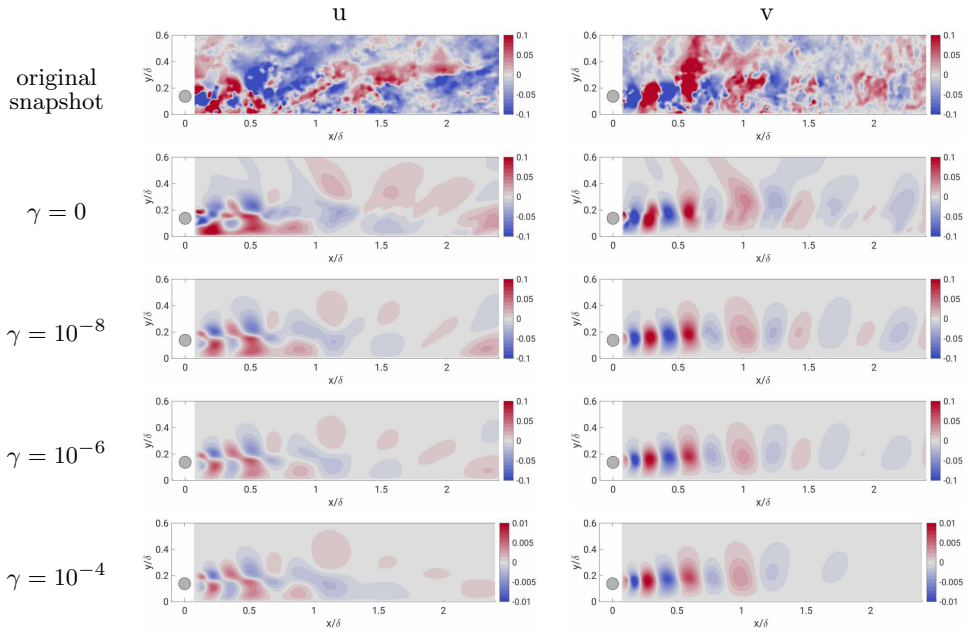



**Fig. 15** Results from a single snapshot (top row) from the D4G4 experiment after projection onto bases of orthogonalized I/O modes. Color contours of streamwise (left column) wall-normal and (right column) velocity perturbation are shown. The second row corresponds to projection on a perfectly orthogonal basis, while the others show the effect of increasing the relaxation parameter $\gamma$.

Finally, Figures 15 and 16 show individual PIV snapshots taken from the D4G4 and D8G4 datasets, respectively, and their projections onto orthogonalized bases of I/O modes. While fine scale turbulence has a strong obscuring effect on the PIV snapshots, the projection procedure is still able to extract coherent flow features associated with vortex shedding in both cases.

Similar to the D4G4 simulation, the wall-normal projections in Figure 15 reveal the presence of a downstream vortex pairing mode in addition to the primary vortex shedding mode upstream. We observe a similar pattern for the experimental results with the smaller cylinder in Figure 16, although the vortex pairing mode does not persist over the full downstream extent of the domain, disappearing by $x/\delta \approx 1$. The D8G4 experiment also seemed to be strongly affected by long streamwise-oriented structures sweeping through the domain that would intermittently increase and decrease the streamwise velocity in the logarithmic region below $y/\delta = 0.2$. The snapshot shown in Figure 16 was acquired at a time when the streamwise velocity over much of this domain was lower than the mean. In this case, while the projections show that streamwise velocity perturbations respond to the modal forcing, the wall-normal velocity perturbations do a much better job at isolating the vortex shedding and pairing modes.

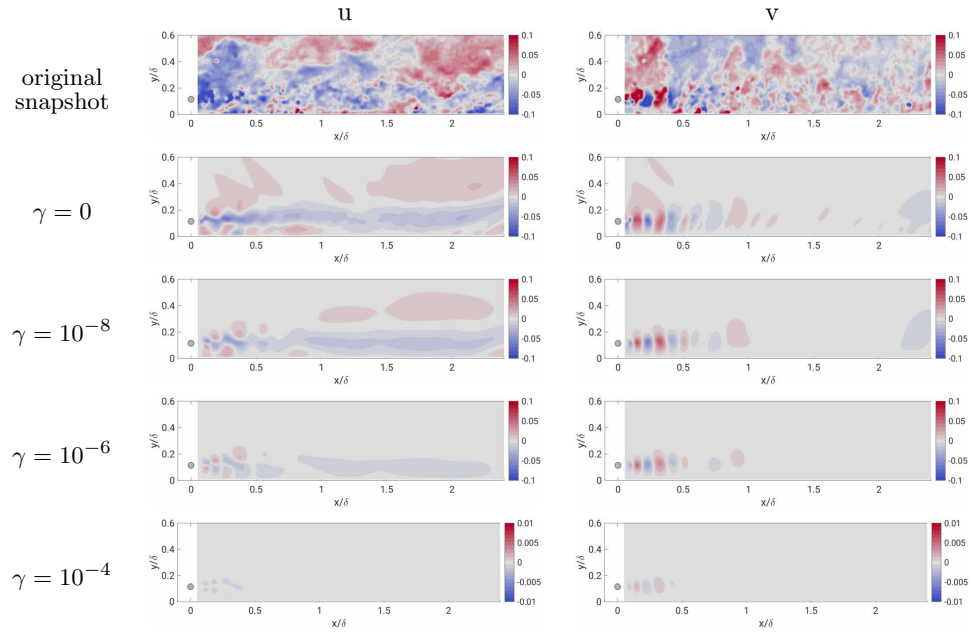



**Fig. 16** Projection of a single snapshot (top row) from the D8G4 experiment after projection onto bases of orthogonalized I/O modes. Color contours of streamwise (left column) wall-normal (right column) velocity perturbation are shown. The second row corresponds to projection on a perfectly orthogonal basis, while the others show the effect of increasing the relaxation parameter $\gamma$.

# 4 Conclusions

We have presented a method for estimating frequency content and associated coherent flow features from temporally uncorrelated PIV snapshots, by projecting them onto orthogonalized bases of I/O modes. Our method extends the idea of Empirical Orthogonal Functions (EOFs) used in reduced-order modeling of fluid flows to find orthogonal bases that not only span the same subspace as the I/O modes, but are also the closest to them in the sense of the $\ell_2$-norm (Löwdin orthogonalization). While EOFs span the I/O mode subspace with a smaller number of modes, they mix different frequencies. By contrast, the basis resulting from Löwdin orthogonalization, which yields a larger number of modes, is useful in partitioning energy among frequencies. This partitioning of energy cannot be done in the original basis of I/O modes because they overlap. In fact, the near linear-dependence of the I/O modes causes the Löwdin basis functions to be highly sensitive to noise. To correct this, we introduce a regularization parameter $\gamma$ to find nearly orthogonal bases close to the original I/O modes. As $\gamma$ increases toward infinity, the resulting basis functions morph from the Löwdin basis functions back to the original I/O basis functions. We find even very small values of $\gamma$ (e.g. $\gamma = 10^{-8}$ in the current flow configuration) to greatly reduce sensitivity of the basis functions to noise while remaining effective at frequency estimation.

We applied our method to snapshots taken from both simulations and experiments of a turbulent boundary layer flowing past a spanwise cylinder. For both cylinder

diameters considered, our method accurately predicted the fundamental frequency and sub-harmonic frequency associated with vortex shedding. In the simulations, phase averaging based on orthogonalized I/O modes also recovered coherent flow features similar to those obtained by SPOD and I/O analysis, especially at the fundamental frequency. Projection of individual snapshots onto orthogonal and nearly-orthogonal bases also revealed a strong vortex shedding mode and vortex pairing downstream. In both experimental configurations, our method predicted vortex shedding frequencies of about $St = 0.2$. Phase-averaging yielded coherent flow features similar to those obtained for the simulations, especially at the fundamental vortex shedding frequency. Furthermore, projection onto orthogonalized I/O modes revealed significant structure in individual PIV snapshots, including not only vortex shedding but also downstream pairing.

As a post-processing tool, our method of frequency estimation and phase averaging is both simple to implement and computationally efficient. The most computationally intensive part of the process is calculating the I/O modes for the original basis. After orthogonalization, I/O modes enable frequency estimation and the extraction of phase averages from sets of temporally uncorrelated PIV snapshots. As we have shown, this worked well for turbulent boundary layer flow past spanwise cylinders. We expect our method to find application across many potential flow configurations where time-resolved measurements are difficult, even at a single point. For example, high-speed flow applications may include instabilities that occur at hundreds of kilohertz. In such cases, our method would work well to average results acquired across multiple runs of a specific configuration. Finally, our method can be applied to mine historical datasets where the measurements were not time resolved.

## Declarations

**Funding.** JWN gratefully acknowledges support from the Office of Naval Research grant number N00014-23-1-2460.

**Conflict of interest.** The authors declare that they have no conflict of interest.

**Data availability statement.** The datasets generated during and/or analyzed during the current study are available from the authors on reasonable request.

## References

[1] Schmid, P.J.: Dynamic mode decomposition of numerical and experimental data. Journal of Fluid Mechanics **656**, 5–28 (2010) https://doi.org/10.1017/S0022112010001217

[2] Towne, A., Schmidt, O.T., Colonius, T.: Spectral proper orthogonal decomposition and its relationship to dynamic mode decomposition and resolvent analysis. Journal of Fluid Mechanics **847**, 821–867 (2018) https://doi.org/10.1017/jfm.2018.283

[3] Theofilis, V.: Global linear instability. Annual Review of Fluid Mechanics **43**, 319–352 (2011)

[4] McKeon, B.J., Sharma, A.S.: A critical-layer framework for turbulent pipe flow. Journal of Fluid Mechanics **658**, 336–382 (2010) https://doi.org/10.1017/S002211201000176X

[5] Jeun, J., Nichols, J.W., Jovanović, M.R.: Input-output analysis of high-speed axisymmetric isothermal jet noise. Physics of Fluids **28**(4), 047101 (2016) https://doi.org/10.1063/1.4946886

[6] Cook, D.A., Nichols, J.W.: Three-dimensional receptivity of hypersonic sharp and blunt cones to free-stream planar waves using hierarchical input-output analysis. Physical Review Fluids **9**, 063901 (2024)

[7] Zare, A., Jovanović, M.R., Georgiou, T.T.: Colour of turbulence. Journal of Fluid Mechanics **812**, 636–680 (2017) https://doi.org/10.1017/jfm.2016.682

[8] Towne, A., Lozano-Durán, A., Yang, X.: Resolvent-based estimation of space–time flow-statistics. Journal of Fluid Mechanics **883**, 17 (2020) https://doi.org/10.1017/jfm.2019.854

[9] Saxton-Fox, T., Lozano-Durán, A., McKeon, B.J.: Amplitude and wall-normal distance variation of small scales in turbulent boundary layers. Phys. Rev. Fluids **7**, 014606 (2022) https://doi.org/10.1103/PhysRevFluids.7.014606

[10] Hussain, A.K.M.F., Reynolds, W.C.: The mechanics of an organized wave in turbulent shear flow. Journal of Fluid Mechanics **41**(2), 241–258 (1970) https://doi.org/10.1017/S0022112070000605

[11] Jordan, P., Colonius, T.: Wave packets and turbulent jet noise. Annual Review of Fluid Mechanics **45**(Volume 45, 2013), 173–195 (2013) https://doi.org/10.1146/annurev-fluid-011212-140756

[12] Discetti, S., Raiola, M., Ianiro, A.: Estimation of time-resolved turbulent fields through correlation of non-time-resolved field measurements and time-resolved point measurements. Experimental Thermal and Fluid Science **93**, 119–130 (2018)

[13] Jin, X., Laima, S., Chen, W.-L., Li, H.: Time-resolved reconstruction of flow field around a circular cylinder by recurrent neural networks based on non-time-resolved particle image velocimetry measurements. Experiments in Fluids **61**(4), 114 (2020)

[14] Zhang, Y., Cattafesta III, L.N., Ukeiley, L.: Spectral analysis modal methods (samms) using non-time-resolved piv. Experiments in Fluids **61**(11), 226 (2020)

[15] Beneddine, S., Yegavian, R., Sipp, D., Leclaire, B.: Unsteady flow dynamics reconstruction from mean flow and point sensors: an experimental study. Journal of Fluid Mechanics **824**, 174–201 (2017)

[16] Symon, S., Sipp, D., McKeon, B.J.: A tale of two airfoils: resolvent-based modelling of an oscillator versus an amplifier from an experimental mean. Journal of Fluid Mechanics **881**, 51–83 (2019)

[17] Berkooz, G., Holmes, P., Lumley, J.L.: The proper orthogonal decomposition in the analysis of turbulent flows. Annual Review of Fluid Mechanics **25**(Volume 25, 1993), 539–575 (1993) https://doi.org/10.1146/annurev.fl.25.010193.002543

[18] Heidt, L., Colonius, T.: Spectral proper orthogonal decomposition of harmonically forced turbulent flows. Journal of Fluid Mechanics **985**, 42 (2024) https://doi.org/10.1017/jfm.2024.70

[19] Borra, A., Flynn, Z., Goza, A., Saxton-Fox, T.: Intrinsic phase-based proper orthogonal decomposition (iphab pod): a method for physically interpretable modes in near-periodic systems. Journal of Fluid Mechanics **1002**, 18 (2025) https://doi.org/10.1017/jfm.2024.1061

[20] Tee, Y.H., Longmire, E.K.: Effect of fluid motions on finite spheres released in turbulent boundary layers. Journal of Fluid Mechanics **985**, 28 (2024)

[21] Chorin, A.J.: Numerical solution of the navier-stokes equations. Math. Comp. **22**, 745–762 (1968) https://doi.org/10.1090/S0025-5718-1968-0242392-2

[22] Mittal, R., Iaccarino, G.: Immersed boundary methods. Annual Review of Fluid Mechanics **37**, 239–261 (2005) https://doi.org/10.1146/annurev.fluid.37.061903.175743

[23] Jovanović, M.R.: From bypass transition to flow control and data-driven turbulence modeling: An input–output viewpoint. Annual Review of Fluid Mechanics **53**(Volume 53, 2021), 311–345 (2021) https://doi.org/10.1146/annurev-fluid-010719-060244

[24] Sharma, A.S., McKeon, B.J.: Closing the loop: an explicit calculation of the nonlinearity in the resolvent formulation of wall turbulence. (2013). https://doi.org/10.2514/6.2013-3118

[25] Huang, Y., Toedtli, S.S., Chini, G.P., McKeon, B.J.: Spatiotemporal characterization of nonlinear forcing and response in turbulent channel flow. Journal of Fluid Mechanics **1035**, 37 (2026) https://doi.org/10.1017/jfm.2026.11540

[26] Pickering, E., Rigas, G., Schmidt, O.T., Sipp, D., Colonius, T.: Optimal eddy viscosity for resolvent-based models of coherent structures in turbulent jets. Journal of Fluid Mechanics **917**, 29 (2021) https://doi.org/10.1017/jfm.2021.232

[27] Reynolds, W.C., Hussain, A.K.M.F.: The mechanics of an organized wave in turbulent shear flow. part 3. theoretical models and comparisons with experiments. Journal of Fluid Mechanics **54**(2), 263–288 (1972) https://doi.org/10.1017/S0022112072000679

[28] Park, D., Mani, A.: Direct calculation of the eddy viscosity operator in turbulent channel flow at $re_\tau = 180$. Journal of Fluid Mechanics **998**, 33 (2024) https://doi.org/10.1017/jfm.2024.660

[29] Welch, P.: The use of fast fourier transform for the estimation of power spectra: A method based on time averaging over short, modified periodograms. IEEE Transactions on Audio and Electroacoustics **15**(2), 70–73 (1967) https://doi.org/10.1109/TAU.1967.1161901

[30] Löwdin, P.: On the non-orthogonality problem connected with the use of atomic wave functions in the theory of molecules and crystals. The Journal of Chemical Physics **18**(3), 365–375 (1950) https://doi.org/10.1063/1.1747632

[31] Dergham, G., Sipp, D., Robinet, J.-C.: Stochastic dynamics and model reduction of amplifier flows: the backward facing step flow. Journal of Fluid Mechanics **719**, 406–430 (2013) https://doi.org/10.1017/jfm.2012.610

[32] Herrmann, B., Baddoo, P.J., Dawson, S.T.M., Semaan, R., Brunton, S.L., McKeon, B.J.: Interpolatory input and output projections for flow control. Journal of Fluid Mechanics **971**, 27 (2023) https://doi.org/10.1017/jfm.2023.680

[33] Farrell, B.F., Ioannou, P.J.: Stochastic forcing of the linearized navier–stokes equations. Physics of Fluids A: Fluid Dynamics **5**(11), 2600–2609 (1993) https://doi.org/10.1063/1.858894

[34] Farrell, B.F., Ioannou, P.J.: Accurate low-dimensional approximation of the linear dynamics of fluid flow. Journal of the Atmospheric Sciences **58**(18), 2771–2789 (2001) https://doi.org/10.1175/1520-0469(2001)0582.0.CO;2

[35] Fey, U., König, M., Eckelmann, H.: A new strouhal–reynolds-number relationship for the circular cylinder in the range 47¡ re¡ 2× 10 5. Physics of Fluids **10**(7), 1547–1549 (1998)

[36] Williamson, C.: Vortex dynamics in the cylinder wake. Annual Review of Fluid Mechanics **28**, 477 (1996)